Chinese Chemical Letters 36 (2025) 110476

Contents lists available at ScienceDirect

Chinese Chemical Letters

journal homepage: www.elsevier.com/locate/cclet

Constant-potential simulation of electrocatalytic N_2 reduction over atomic metal-N-graphene catalysts

Sanmei Wang[a], Yong Zhou[a,*], Hengxin Fang[a], Chunyang Nie[a,*], Chang Q Sun[a,c,d], Biao Wang[a,b,*]

[a] Research Institute of Interdisciplinary Sciences (RISE) and School of Materials Science & Engineering, Dongguan University of Technology, Dongguan 523808, China
[b] Sino-French Institute of Nuclear Engineering and Technology, Sun Yat-sen University, Zhuhai 519082, China
[c] Guangdong Provincial Key Laboratory of Extreme Conditions, Dongguan 523803, China
[d] School of Science, Nanyang Technological University, Singapore 639798, Singapore

ARTICLE INFO

Article history:
Received 1 July 2024
Revised 18 September 2024
Accepted 19 September 2024
Available online 19 September 2024

Keywords:
N_2 reduction
Single-atom catalysts
Constant potential
Graphene
DFT

ABSTRACT

Charge-neutral method (CNM) is extensively used in investigating the performance of catalysts and the mechanism of N_2 electrochemical reduction (NRR). However, disparities remain between the predicted potentials required for NRR by the CNM methods and those observed experimentally, as the CNM method neglects the charge effect from the electrode potential. To address this issue, we employed the constant electrode potential (CEP) method to screen atomic transition metal-N-graphene (M_1/N-graphene) as NRR electrocatalysts and systematically investigated the underlying catalytic mechanism. Among eight types of M_1/N-graphene (M_1 = Mo, W, Fe, Re, Ni, Co, V, Cr), W_1/N-graphene emerges as the most promising NRR electrocatalyst with a limiting potential as low as −0.13 V. Additionally, the W_1/N-graphene system consistently maintains a positive charge during the reaction due to its Fermi level being higher than that of the electrode. These results better match with the actual circumstances compared to those calculated by conventional CNM method. Thus, our work not only develops a promising electrocatalyst for NRR but also deepens the understanding of the intrinsic electrocatalytic mechanism.

Ammonia (NH_3), a crucial compound, serves as fertilizer, chemicals, and a potential medium for hydrogen storage [1–4]. Currently, the Haber–Bosch process is commonly used for industrial NH_3 production, operating at high pressure and temperature (200 atm and 400–450 °C) [5]. This process consumes >1% of the Earth's energy supply and contributes to about 3% of global CO_2 emissions [6,7]. Therefore, exploring alternative pathways for more efficient NH_3 production under milder conditions is urgently needed.

A multitude of innovative approaches have been developed for the conversion of N_2 into NH_3, including biological catalysis [8,9], photocatalysis [10,11], and electrocatalysis [12–15]. Among them, the electrochemical N_2 reduction reaction (NRR) stands out as a highly promising avenue owing to its ability to operate at atmospheric pressure and moderate temperature using renewable electric energy [16–20]. In the electrochemical NRR, the NH_3 yield is mainly governed by the activity of the electrocatalyst and operating parameters such as potential, electrolyte, pH [21]. In recent years, single-atom catalysts (SACs) have emerged as a frontier in catalysis due to their maximized utilization efficiency of metal atoms and tunable electronic properties. Various SACs including Co-, W-, Ni-, Mo-, Fe-, and Cr-based SACs, have been developed for electrocatalytic synthesis of NH_3 [22–25]. Unfortunately, many of these catalysts exhibit a low faradaic efficiency of <50% [17,18,26,27]. Hence, further advancements in NH_3 synthesis using single-atom electrocatalysts necessitate an insightful understanding of the intrinsic catalytic mechanisms. To this end, an accurate atomistic simulation method to provide insights into the NRR processes is essential.

Constant charge density functional theory (DFT) calculations are extensively employed to study the catalytic properties of SACs for NRR [28–30]. These computations generally assume that the catalyst is charge neutral for computational simplicity (known as CNM method). Consequently, the Fermi level of the neutral catalyst changes as the reaction proceeds due to the variation in the adsorbed chemical species. However, in reality, the Fermi level of the catalyst is fixed by the electrode potential. As a result, the system often has net electronic charges changing along the reaction

* Corresponding authors.
E-mail addresses: zhouyong@dgut.edu.cn (Y. Zhou), niechunyang@dgut.edu.cn (C. Nie), wangbiao@mail.sysu.edu.cn (B. Wang).

https://doi.org/10.1016/j.cclet.2024.110476
1001-8417/

coordinate [31,32]. Thus, there is a significant discrepancy between the theoretical potential predicted by the CNM method and the actual potential observed in experiments [18,33,34].

To address this issue, applying constant electrode potential (CEP) method to investigate the electrocatalytic performance of SACs in NRR is a possible solution. The CEP method can automatically adjust the charge of catalyst and ensure that the Fermi level of catalyst consistently aligns with the electrode voltage, which is closer to the actual reaction environment [35,36]. For example, Liu *et al*. applied the CEP method to clearly explain the reversible transformation between copper single atoms and clusters observed in experiments [37]. Gao *et al*. reproduced the macroscopic data (*i.e.*, polarization curves and Tafel slope) of electrochemical experiments on a Pt surface using CEP method [38].

Herein, we employed the CEP method to study the electrocatalytic NRR performances of SACs supported by N-doped graphene (M_1/N-graphene) to comprehensively understand their catalytic properties and underlying mechanisms. N-doped graphene, a two-dimensional material [39–41], is a favored substrate for SACs due to the good ability of lone pair electrons in N atoms for coordinating with metal atoms. Simultaneously, N-graphene features a large specific surface area, high conductivity, and excellent electrochemical stability. In addition, the electronic structures of N-graphene are more susceptible to environmental conditions (*e.g.*, pH, charge, and potential effects) compared to those of three-dimensional metal catalysts [42].

Firstly, we screened eight types of M_1/N-graphene materials (M_1 = Mo, W, Fe, Re, Ni, Co, V, Cr) based on three criteria and identified Mo_1/N-graphene and W_1/N-graphene as potential NRR electrocatalysts. The reason for selecting those metal atoms is because transition metal-based materials have been widely applied for NH_3 synthesis due to their good catalytic activity, resource availability, cost-effectiveness and environmental friendliness [43–46]. Then we systematically compared the electrocatalytic performances between Mo_1/N-graphene and W_1/N-graphene through CEP method and found that W_1/N-graphene exhibits higher NRR activity. The enhanced catalytic activity of W_1/N-graphene is attributed to the stronger interaction between N_2 and W atoms, as well as greater electron transfer from W_1/N-graphene to the antibonding orbital of N_2. Meanwhile, we also calculated the NRR processes on W_1/N-graphene using the CNM method. By comparison, it was discovered that the estimated U_L along the distal pathway is lower and the variations in atomic charges of the catalyst along the distal pathway are more positive in the case of CEP method, which is more consistent with the actual conditions.

Structures of eight types of single metal atoms M_1 (M_1 = Mo, W, Fe, Re, Ni, Co, V, Cr) supported on N-graphene were constructed, as illustrated in Fig. 1a. N_2 adsorption on the catalyst surface served as the initial stage of the NRR process, and its initial adsorption manner (end-on and side-on modes) is pivotal in determining the subsequent reaction. After full structural relaxation, we observed that the end-on configuration has a stronger adsorption energy than the side-on mode (Fig. 1b), indicating that N_2 favors end-on adsorption mode. Thus, we will exclusively focus on the end-on adsorption mode of N_2, and the subsequently mentioned adsorption energy refers specifically to the end-on mode.

We further compared the adsorption energies of hydrogen and N_2 to evaluate whether N_2 can be effectively captured by metal active sites. Fig. S1 (Supporting information) shows that N_2 exhibits higher binding energies compared to hydrogen for all structures. This suggests that the competitive hydrogenation evolution reaction would be suppressed, thereby potentially increasing the surface concentration of N_2 and facilitating subsequent NRR. Furthermore, we calculated the adsorption energies of hydrogen and N_2 using CNM methods, as depicted in Fig. S2 (Supporting information). CNM methods also reveal a higher binding energy for N_2 compared to hydrogen. However, the adsorption energies of N_2 and hydrogen calculated by CEP methods are weaker than those obtained with CNM methods due to the neglect of surface charge effects in CNM methods. The influence of surface charge on the adsorption strength of both N_2 and hydrogen onto M_1/N-graphene is possibly attributed to the reason that the surface charge can alter the electronic state occupation and thus affect the adsorption of N_2 [36].

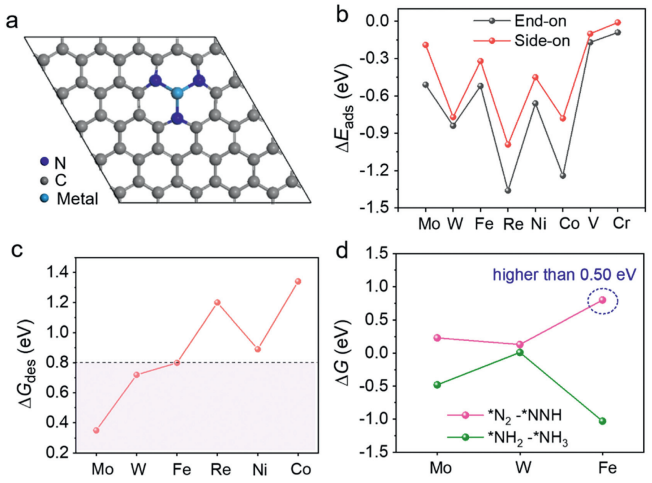

Fig. 1. (a) Structures of single metal atoms supported on N-graphene. (b) Adsorption energy of N_2 with end-on and side-on modes on various metal atoms. (c) Desorption free energy (ΔG_{des}) of NH_3 on various SACs. (d) The free energy barriers (ΔG) for the hydrogenation of $^*N_2$ to $^*NNH$ and the hydrogenation of $^*NH_2$ to $^*NH_3$.

According to previous investigations, three criteria can be used to screen NRR electrocatalysts [30,47]: (1) The adsorption energy (ΔE_{ads}) of N_2 should be more negative than −0.50 eV to activate its inert N≡N triple bond sufficiently; (2) the desorption free energy of $^*NH_3$ should not exceed 0.80 eV to guarantee the reduction of the overpotential; and (3) the free energy barriers for the hydrogenation of $^*N_2$ into $^*NNH$ and the hydrogenation of $^*NH_2$ into $^*NH_3$ should be lower than 0.50 eV. The reason for choosing these two steps is that the first protonation ($^*N_2 + H^+ + e^- \rightarrow {}^*NNH$) and the last protonation step ($^*NH_2 + H^+ + e^- \rightarrow {}^*NH_3$) are responsible for the relatively high energy barrier of the NRR process. The first protonation reaction converts stable $^*N_2$ into the unstable $^*NNH$, requiring a significant amount of energy to break the strong N≡N triple bonds. This process is thermodynamically unfavorable with a positive change in free energy. Similarly, the transition from the stable $^*NH_2$ moiety to the much less stable $^*NH_3$ intermediate always necessitates a relatively high energy input. All remaining reaction steps are typically thermodynamically favorable.

According to the above criteria, we screened a series of M_1/N-graphene using CEP methods. Following criterion 1, we compared ΔE_{ads} of N_2 on various structures (Fig. 1b). Except for the anchored V and Cr atoms, the ΔE_{ads} values for N_2 adsorption on other metals are below −0.50 eV. This indicates that V and Cr atoms are not suitable as NRR electrocatalysts due to their poor performance in N_2 activation. Following criterion 2, it is evident that Re_1/N-graphene, Ni_1/N-graphene, and Co_1/N-graphene are also not suitable for NRR due to their relatively strong interaction with $^*NH_3$ species, with desorption free energies of 1.20, 0.89, and 1.34 eV, respectively (Fig. 1c). Finally, Fe_1/N-graphene is excluded as an electrocatalyst candidate according to criterion 3 because of its relatively high energy barrier of >0.50 eV for the hydrogenation of $^*N_2$ into $^*NNH$ (Fig. 1d).

In addition, we investigated the relationship between the adsorption energy of N_2 and the degree of N_2 activation over various M_1/N-graphene by conducting linear fittings between adsorp-

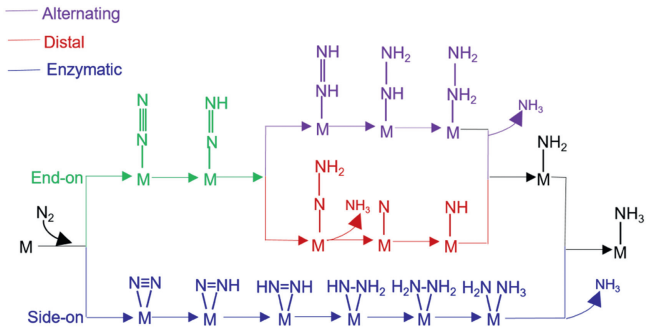

Fig. 2. Schematic depiction of three mechanisms for N_2 electroreduction to NH_3 on M_1/N-graphene.

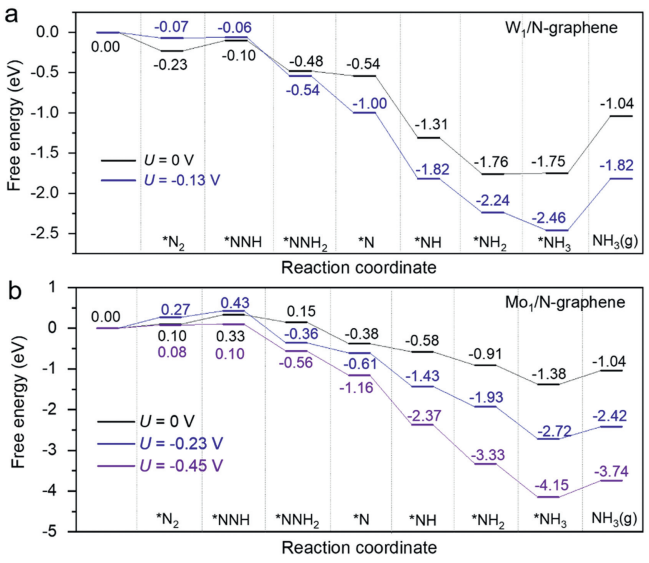

Fig. 3. Gibbs free energy diagrams for electrochemical NRR on (a) W_1/N-graphene and (b) Mo_1/N-graphene along the distal pathways. The temperature used for calculating Gibbs free energy was 298.15 K.

tion energy and the N-N bond length in $*N_2$ and *NNH species. As shown in Fig. S3a (Supporting information), the adsorption energy of N_2 is linearly related to the N-N bond length of $*N_2$, while no linear correlation is observed for the N-N bond length of *NNH (Fig. S3b in Supporting information). Specifically, the N-N bond length in $*N_2$ elongates with the increase of adsorption energy of N_2, signifying a higher degree of activation of N_2.

Based on the above discussion, we conclude that W_1/N-graphene and Mo_1/N-graphene are supposed to serve as promising NRR electrocatalysts. Thus, we will further investigate the whole reaction pathways of electrochemical NRR on W_1/N-graphene and Mo_1/N-graphene. Fig. 2 illustrates all proposed reaction pathways for NRR, encompassing distal, alternating, and enzymatic mechanisms. Each mechanism involves the transfer of six protons and six electrons. Since the N_2 adsorption on W_1/N-graphene and Mo_1/N-graphene favors end-on modes, the NRR processes on W_1/N-graphene and Mo_1/N-graphene tend to follow distal or alternating pathways.

The computed Gibbs free energy profiles of distal pathways on W_1/N-graphene and Mo_1/N-graphene using the CEP method are depicted in Figs. 3a and b, respectively, and the corresponding results of alternating pathways are shown in Figs. S4 and S5 (Supporting information), respectively. For W_1/N-graphene, the distal pathways manifest lower energies than the alternating pathways, suggesting that NRR on W_1/N-graphene should follow the distal pathways. In the distal pathways, under the condition of $U = 0$ V, the adsorbed $*N_2$ undergoes hydrogenation through proton-coupled electron transfer, forming an *NNH species adsorbed on the W sites. The H atoms are bonded to the distal N site with a N–H bond length measured at 1.04 Å, while the N–N bond extends to 1.23 Å. This step exhibits a slight increase in the free energy by 0.13 eV. Subsequently, a proton-coupled electron sequentially attacks the distal N atom of the *NNH species. This leads to the formation of the $*NNH_2$ species, accompanied by a decrease in Gibbs free energy of 0.38 eV.

Then the third proton-coupled electron interacts with the pre-hydrogenated N site of the $*NNH_2$ species. After that, the first NH_3 is released, leaving one N atom on W with a W–N length of 1.72 Å. The transformation from $*NNH_2$ to $NH_3 + *N$ involves a downhill free energy change of 0.06 eV. In the subsequent stage, the remaining *N species undergo continuous hydrogenation to *NH, $*NH_2$, and $*NH_3$ species, with free energy changes of −0.77, −0.45, and 0.01 eV, respectively, leading to the formation of the second NH_3. The second NH_3 desorbs from the W sites, necessitating an energy input of 0.71 eV. Remarkably, the limiting-potential step of NRR on W_1/N-graphene along the distal pathway at $U = 0$ V is the first protonation of $*N_2$ to form the *NNH species, with a reaction Gibbs free energy of 0.13 eV. The limiting potentials (U_L) *versus* the reverse hydrogen electrode (RHE) on W_1/N-graphene are calculated to be −0.13 V according to $U_L = -\Delta G_L/e$, where ΔG_L represents the reaction Gibbs free energy of the limiting potential step.

We further investigated the processes of NRR on W_1/N-graphene at $U = -0.13$ V using the CEP method (Fig. 3a). It is observed that along the distal pathway, all elementary steps are downhill except for the conversion from $*N_2$ to *NNH, which has a reaction Gibbs free energy of 0.01 eV, approximately equivalent to no barrier. These results indicate that −0.13 V effectively drive the NRR. For comparison, we also performed calculations using the CNM method. The results derived from the CNM method show that, under the condition of $U = 0$ V, the limiting-potential step for NRR on W_1/N-graphene along the distal pathway is the last protonation of $*NH_2$ to $*NH_3$, with a reaction Gibbs free energy of 0.67 eV (Fig. S6 in Supporting information). The U_L of −0.67 V calculated by CNM methods exceeds that calculated by the CEP method (−0.13 V). Yu's work also demonstrated that the calculated limiting potential by the CNM method for the Fe-N-C catalyst in the oxygen reduction reaction (−1.0 V *vs.* RHE) surpasses the applied potential in the experiments (−0.40 V *vs.* RHE) [36]. Thus, we speculate that the U_L on W_1/N-graphene calculated by the CEP method is closer to the actual potential for triggering N_2 reduction.

For Mo_1/N-graphene, distal pathways exhibit lower energy than alternating pathways, suggesting that NRR on Mo_1/N-graphene also follows the distal pathways (Fig. 3b and Fig. S5). Under the condition of $U = 0$ V, the conversion from $*N_2$ to *NNH is a non-spontaneous process with a relatively positive free energy of 0.23 eV. The subsequent generations of $*NNH_2$, *N, *NH, $*NH_2$, and $*NH_3$ are spontaneous processes with free energies of −0.18, −0.53, −0.20, −0.33, and −0.47 eV, respectively. Thus, the limiting step of NRR on Mo_1/N-graphene in distal pathways is the first protonation of N_2 to form the NNH* species with an energy barrier of 0.23 eV. We also performed linear fitting between the adsorption energy of N_2 and the N-N bond length in $*NNH_2$ for all M_1/N-graphene catalysts. It can be seen from Fig. S3c (Supporting information) that no linear correlation exists between the two factors. Furthermore, we examined whether a potential of −0.23 V could drive the occurrence of distal pathways on Mo_1/N-graphene. Upon applying $U = -0.23$ V, all elementary steps exhibit a downhill trend except for the transformation from $*N_2$ to *NNH, which has a reaction Gibbs free energy of 0.16 eV. These results suggest that −0.23 V is insufficient to drive this process. Consequently, we attempted to increase the electric potential to −0.45 V. The results indicate that the energy barrier of the limiting step for NRR decreases to

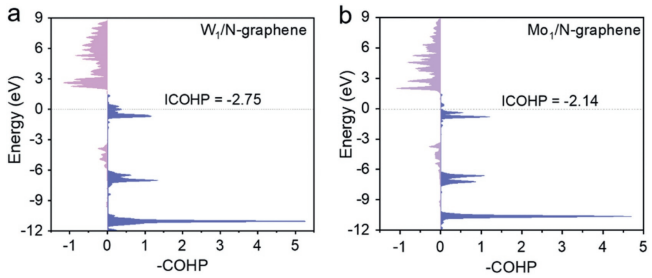

Fig. 4. The crystal orbital Hamilton population between adsorbed N_2 and the active sites on (a) W_1/N-graphene and (b) Mo_1/N-graphene.

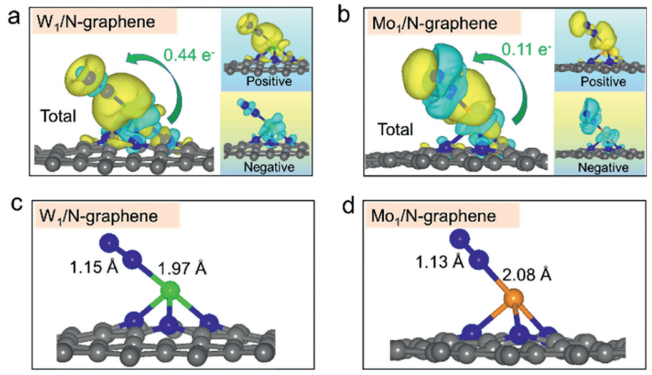

Fig. 5. Difference charge density diagrams of adsorbed N_2 on (a) W_1/N-graphene and (b) Mo_1/N-graphene. The optimal structures of the adsorbed N_2 on (c) W_1/N-graphene and (d) Mo_1/N-graphene.

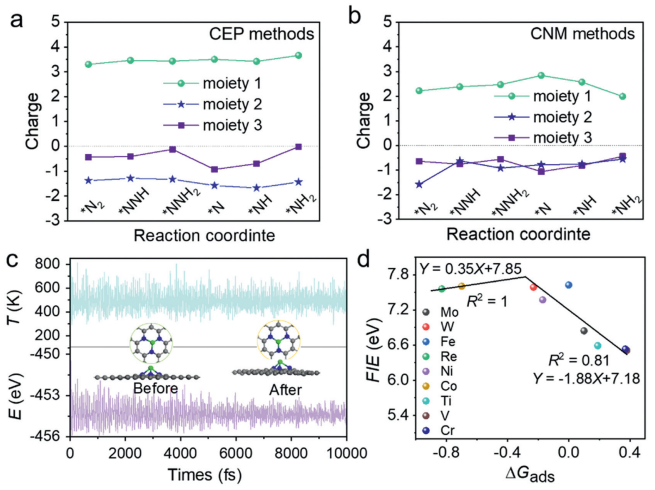

Fig. 6. Charge variation of the graphene (moiety 1), W_1-N_3 (moiety 2), N_xH_y species (moiety 3) on W_1/N-graphene at different species states along the minimum Gibbs free energy surface, calculated by (a) constant-potential DFT and (b) CNM methods. (c) *Ab initio* molecular dynamics simulations of W_1/N-graphene with variations in temperature (T) and energy (E) at 500 K, with a time-step of 1 fs. The inserts show top and side views of the atomic configuration snapshot before and after the *ab initio* molecular dynamics simulation. (d) The relationship between the first ionization energy (*FIE*) of metals and the adsorption free energy (ΔG_{ads}) of N_2.

0.02 eV, which is roughly equivalent to no barrier. Hence, we deduce that the minimum potential required to drive the NRR reaction on Mo_1/N-graphene is −0.45 V.

From the above discussion, we know that the electrode potential required for W_1/N-graphene to drive the NRR reaction is lower than that for Mo_1/N-graphene, which indicates higher electrocatalytic activity for W_1/N-graphene. To further understand the superior catalytic activity of W_1/N-graphene to Mo_1/N-graphene, we performed crystal orbital Hamilton population (COHP) analysis [48,49] between single metal atoms and the N atoms of adsorbed N_2 to assess the interaction between N_2 and the active sites at 0 V. As illustrated in Fig. 4, the COHP diagram shows positive peaks with a certain height below the Fermi level, indicating that the electrons of Mo and W may fill the antibonding orbitals of N_2 to a certain extent. Besides, the integrated COHP (ICOHP) between the atomic metal site and the N atom of adsorbed N_2 in W_1/N-graphene is approximately −2.75 eV, which is more negative than that of Mo_1/N-graphene (−2.14 eV). This suggests that W_1/N-graphene manifests a stronger interaction with N_2 compared to Mo_1/N-graphene. Furthermore, we computed the charge density difference, Bader charge, and bond length of the adsorbed N_2 using CEP method. The charge density difference reveals a charge transfer between the adsorbed N_2 and the catalyst (Figs. 5a and b). Specifically, the amounts of charge transferred from W_1/N-graphene and Mo_1/N-graphene to N_2 are 0.44 and 0.11 e, respectively. This means that W_1/N-graphene donates more electrons to the antibonding orbital of N_2 than Mo_1/N-graphene. Furthermore, the N≡N bond length on W_1/N-graphene elongates from 1.11 Å (in the gas phase) to 1.15 Å, surpassing the length of the N≡N bond on Mo_1/N-graphene (1.13 Å) (Figs. 5c and d). Notably, the U_L of W_1/N-graphene (−0.13 V) is comparable to that of B_2–5-Ti_2@C_2N (−0.10 V) which is also predicted to be a promising NRR electrocatalyst [50]. The slight difference in U_L between the two catalysts should be ascribed to the distinct structural compositions, active sites, and employed computational methods. Specifically, B_2–5-Ti_2@C_2N behaves as the double-atom catalysts, while W_1/N-graphene behaves as the SACs. In addition, the U_L of B_2–5-Ti_2@C_2N was calculated using the CNM method rather than CEP method.

The variations in atomic charges during each elementary step along the favorable distal pathway under the condition of $U = 0$ V were examined. According to previous studies [51], the W_1/N-graphene system is categorized into three moieties: moiety 1 (graphene monolayer), moiety 2 (W_1-N_3, composed of W and its surrounding three N atoms), and moiety 3 (the adsorbed N_xH_y species). In the CEP method, as illustrated in Fig. 6a, $^*N_2$, $^*NNH$, $^*NNH_2$, $^*N$, and $^*NH$ species on W_1/N-graphene gain electrons, while $^*NH_2$ neither gains nor loses electrons. W_1-N_3 always gains electrons, and graphene always loses electrons. The reason why $^*NH_2$ neither gains nor loses electrons is assumably because the electron loss of graphene and electron gain of W_1-N_3 are sufficient to maintain U at 0 V, which makes $^*NH_2$ neither gain or lose electrons. It is worth noting that the sum of the charges of moieties 1, 2, and 3 always exhibits a positive charge. The reason for this is that the Fermi level of W_1/N-graphene in its charge-neutral state is higher than the electrode potential. To align the Fermi levels, W_1/N-graphene had to lose electrons, thus acquiring a positive charge. This result is in line with a recent theoretical study reporting that the higher E_F of the surface of N-doped graphene supported Fe SAC than the electrode potential causes the Fe SAC surface to acquire a positive charge under $U = 0.50$ V [36]. Nevertheless, this positive charge phenomenon is not observed in CNM simulations, as the method neglects charge effects, resulting in the sum of the charges of moieties 1, 2, and 3 always being zero (Fig. 6b).

To assess the stability of W_1/N-graphene and Mo_1/N-graphene, we performed ab initio molecular dynamics simulations at 500 K. The geometric structures of both W_1/N-graphene and Mo_1/N-graphene have no significant distortion during the simulation, indicative of their high thermodynamic stability (Fig. 6c and Fig. S7 in Supporting information).

Currently, large-scale materials screening for NRR catalysts is largely hindered by expensive costs. To reduce these screening

costs and improve efficiency, we attempt to find a suitable descriptor to replace the calculations. Fig. 6d shows the relationship between the first ionization energy of metals and the ΔG_{ads} of N_2, revealing a clear volcano curve. Among nine structures, W_1@N-graphene is predicted to have the best catalytic activity in the NRR process, corresponding to its adsorption free energy for N_2 being closest to the peak of the volcano. Thus, the first ionization energies of metals obtained from the database can serve as a valuable descriptor for predicting the catalytic performance of catalysts, thereby reducing costs and accelerating the discovery of catalysts for NRR.

In conclusion, we investigated the impact of charges on electrocatalytic NRR using the CEP method, aiming to reconcile discrepancies observed between experimental results and conventional charge-neutral DFT calculations. Atomic M_1-N-graphene catalysts were selected as the model NRR electrocatalysts. The calculations derived from CEP method reveal that W_1/N-graphene stands out among eight types of atomic M_1-N-graphene structures, exhibiting a U_L of −0.13 V along the distal pathway. The high catalytic activity of W_1/N-graphene is attributed to the stronger interaction between N_2 and W atoms, as well as the enhanced electron transfer from W_1/N-graphene to N_2. Furthermore, the W_1/N-graphene system consistently maintains a positive charge during the reaction due to its higher Fermi level compared to the electrode. These phenomena cannot be accessed using CNM simulations. Thus, our work deepens the understanding of the electrocatalytic mechanisms of NRR by incorporating the charge effects and offers guidelines for designing superior NRR electrocatalysts.

Declaration of competing interest

The authors declare that they have no known competing financial interests or personal relationships that could have appeared to influence the work reported in this paper.

CRediT authorship contribution statement

Sanmei Wang: Writing – original draft, Methodology, Investigation, Data curation, Conceptualization. **Yong Zhou:** Writing – review & editing, Supervision. **Hengxin Fang:** Visualization, Data curation. **Chunyang Nie:** Writing – review & editing, Supervision. **Chang Q Sun:** Writing – review & editing. **Biao Wang:** Writing – review & editing.

Acknowledgments

Financial support from Natural Science Foundation of Guangdong Province (No. 2024A1515011094 (C.Q Sun)) and National Natural Science Foundation of China (Nos. 12304243 (H.X. Fang), 12150100 (B. Wang)) is gratefully acknowledged.

Supplementary materials

Supplementary material associated with this article can be found, in the online version, at doi:10.1016/j.cclet.2024.110476.

References

[1] N. Gruber, J.N. Galloway, Nature 451 (2008) 293–296.
[2] L.F. Greenlee, Nat. Energy 5 (2020) 557–558.
[3] D.R. MacFarlane, P.V. Cherepanov, J. Choi, et al., Joule 4 (2020) 1186–1205.
[4] C. Tang, S.Z. Qiao, Joule 3 (2019) 1573–1575.
[5] J.N. Galloway, A.R. Townsend, J.W. Erisman, et al., Science 320 (2008) 889–892.
[6] J.W. Erisman, M.A. Sutton, J. Galloway, et al., Nat. Geosci. 1 (2008) 636–639.
[7] R. Schlögl, Angew. Chem. Int. Ed. 42 (2003) 2004–2008.
[8] C. Liu, K.K. Sakimoto, B.C. Colón, et al., Proc. Natl. Acad. Sci. U. S. A. 114 (2017) 6450–6455.
[9] K.T. Shanmugam, R.C. Valentine, Proc. Natl. Acad. Sci. U. S. A. 72 (1975) 136–139.
[10] Y. Xiong, B. Li, Y. Gu, et al., Nat. Chem. 15 (2023) 286–293.
[11] W. Zhang, T. Liu, Q. Tan, et al., ACS Catal. 13 (2023) 3242–3253.
[12] G.F. Chen, Y. Yuan, H. Jiang, et al., Nat. Energy 5 (2020) 605–613.
[13] K. Qi, X.Q. Cui, L. Gu, et al., Nat. Commun. 10 (2019) 5.
[14] J. Wang, M. Shi, G. Yi, et al., Chin. Chem. Lett. 33 (2022) 4623–4627.
[15] C. Cai, K. Liu, L. Zhang, et al., Angew. Chem. Int. Ed. 62 (2023) e202300873.
[16] Y. Wang, W. Zhou, R. Jia, et al., Angew. Chem. Int. Ed. 59 (2020) 5350–5354.
[17] X. Li, P. Shen, Y. Luo, et al., Angew. Chem. Int. Ed. 61 (2022) e202205923.
[18] F. Lü, S. Zhao, R. Guo, et al., Nano Energy 61 (2019) 420–427.
[19] Y. Zhao, S. Zhang, C. Han, et al., Chem. Eng. J. 468 (2023) 143517.
[20] W. Zang, T. Yang, H. Zou, et al., ACS Catal. 9 (2019) 10166–10173.
[21] H.P. Jia, E.A. Quadrelli, Chem. Soc. Rev. 43 (2014) 547–564.
[22] S. Zhang, M. Jin, T. Shi, et al., Angew. Chem. Int. Ed. 59 (2020) 13423–13429.
[23] L. Han, X. Liu, J. Chen, et al., Angew. Chem. Int. Ed. 58 (2019) 2321–2325.
[24] L. Chen, C. He, R. Wang, et al., Chin. Chem. Lett. 32 (2021) 53–56.
[25] J. Guo, T. Tadesse Tsega, I. Ul Islam, et al., Chin. Chem. Lett. 31 (2020) 2487–2490.
[26] Y. Ma, T. Yang, H. Zou, et al., Adv. Mater. 32 (2020) 2002177.
[27] J. Chen, Y. Kang, W. Zhang, et al., Angew. Chem. Int. Ed. 61 (2022) e202203022.
[28] H. Yin, S.L. Li, L.Y. Gan, P. Wang, J. Mater. Chem. A 7 (2019) 11908–11914.
[29] N. Saeidi, M.D. Esrafili, J.J. Sardroodi, ChemistrySelect 4 (2019) 12216–12226.
[30] P. Ou, X. Zhou, F. Meng, et al., Nanoscale 11 (2019) 13600–13611.
[31] S. Surendralal, M. Todorova, M.W. Finnis, J. Neugebauer, Phys. Rev. Lett. 120 (2018) 246801.
[32] G. Kastlunger, P. Lindgren, A.A. Peterson, J. Phys. Chem. C 122 (2018) 12771–12781.
[33] C. He, Z.Y. Wu, L. Zhao, et al., ACS Catal. 9 (2019) 7311–7317.
[34] Y. Wang, X. Cui, J. Zhao, et al., ACS Catal. 9 (2019) 336–344.
[35] X. Zhao, Y. Liu, J. Am. Chem. Soc. 143 (2021) 9423–9428.
[36] S. Yu, Z. Levell, Z. Jiang, et al., J. Am. Chem. Soc. 145 (2023) 25352–25356.
[37] X. Bai, X. Zhao, Y. Zhang, et al., J. Am. Chem. Soc. 144 (2022) 17140–17148.
[38] G. Gao, L.W. Wang, Chem. Catal. 1 (2021) 1331–1345.
[39] C. He, J. Ma, S. Xi, W. Zhang, J. Energy Chem. 97 (2024) 68–78.
[40] C. He, S. Yan, W. Zhang, J. Energy Chem. 96 (2024) 437–447.
[41] C. He, J. Ma, Y. Wu, W. Zhang, J. Energy Chem. 84 (2023) 131–139.
[42] D. Kim, J. Shi, Y. Liu, J. Am. Chem. Soc. 140 (2018) 9127–9131.
[43] S. Chung, H. Ju, M. Choi, et al., Angew. Chem. Int. Ed. 61 (2022) e202212676.
[44] N. Zhang, A. Jalil, D. Wu, et al., J. Am. Chem. Soc. 140 (2018) 9434–9443.
[45] Z.Y. Wu, M. Karamad, X. Yong, et al., Nat. Commun. 12 (2021) 2870.
[46] T.N. Ye, S.W. Park, Y. Lu, et al., Nature 583 (2020) 391–395.
[47] C. Ling, Y. Ouyang, Q. Li, et al., Small Methods 3 (2019) 1800376.
[48] C. He, C. Xu, W. Zhang, ACS Appl. Mater. Interfaces 15 (2023) 57015–57028.
[49] Y. Wu, C. He, W. Zhang, J. Am. Chem. Soc. 144 (2022) 9344–9353.
[50] S. Han, X. Wei, Y. Huang, et al., Nano Energy 99 (2022) 107363.
[51] X. Zhai, L. Li, X. Liu, et al., Nanoscale 12 (2020) 10035–10043.